Supporting Information

for

Crystallization Pathways and Hydrogen-Bond Topology Program Spin Crossover in Interconverting Fe(II)-Complex Polymorphs

Jia-Qing Zhang, Jie-Sheng Hu, Xin-Li Shi, Ai-Wen Ge, Yu-Xiao Chen, Jia-Hui Zhang, Zi-Shuo Yao, Meng Yu,* Jun Tao*

Key Laboratory of Cluster Science of Ministry of Education, School of Chemistry and Chemical Engineering, Liangxiang Campus, Beijing Institute of Technology, Beijing 102488, People's Republic of China. E-mail: mengyu@bit.edu.cn; taojun@bit.edu.cn

Table of Contents

1. Experimental Section

1.1 Materials

All reagents and solvents were purchased from commercial sources and used as received without any further purification. 6-Methyl-2-pyridinecarboxaldehyde, thiosemicarbazide, L-ascorbic acid, and tetrafluoroterephthalic acid were purchased from Adamas-beta (Shanghai, China); $Fe(ClO_4)_2 \cdot 6H_2O$ from Meryer (Shanghai, China); methanol from Greagent (Shanghai, China); and triethylamine and diethyl ether from Beijing Tong Guang Fine Chemicals Company (Beijing, China).

1.2 Synthesis

Synthesis of 6-methyl-2-formylpyridine thiosemicarbazone (HL)

6-methyl-2-formylpyridine thiosemicarbazone hydrate (**HL·H_2O**) was synthesized according to reference.[1] Briefly, 6-methyl-2-pyridinecarboxaldehyde (5.0 g, 41.3 mmol) and thiosemicarbazide (3.71 g, 41.3 mmol) were dissolved in methanol (100 mL), to this solution two drops of acetic acid were added. The solution was then stirred and heated to 70 °C, after refluxed for 12 h the solution was allowed to stand at room temperature for solvent evaporation. Light yellow-fluffy crystals of **HL·H_2O** (5.7 g, 65.7%) were obtained after 2 days.

Synthesis of $[Fe(HL)_2](4FTPA)\cdot 2.5H_2O$ (4F-1)

HL·H_2O (42 mg, 0.20 mmol), L-ascorbic acid (17 mg, 0.10 mmol), and $Fe(ClO_4)_2 \cdot 6H_2O$ (32 mg, 0.09 mmol) were dissolved in methanol (5 mL) under a nitrogen atmosphere and stirred for 30 min to give solution A. In parallel, tetrafluoroterephthalic acid (H_2[4FTPA]; 24 mg, 0.1 mmol) was dissolved in water (4 mL), and triethylamine (27.6 μL) was added to give solution B. Solution B was then added to solution A under N_2, and diethyl ether was allowed to slowly diffuse into the mixture. Black plate-like crystals appeared within minutes, and crystals suitable for single-crystal X-ray diffraction were obtained after ca. 16 h (17.0 mg, isolated in 26.0% yield based on Fe). Because **4F-1** is an intermediate crystalline phase in the crystallization sequence, the isolated yield is sensitive to the sampling time. Anal. $C_{24}H_{25}F_4FeN_8O_{6.5}S_2$ (725.49); calcd: C, 39.73; H, 3.47; N, 15.45; found: C, 39.35; H, 3.36; N, 15.48.

Synthesis of $[Fe(HL)_2](4FTPA)$ (4F-2; solvate phase with unresolved lattice solvent)

4F-2 could also be obtained from the same crystallization conditions as for **4F-1**, indicating that **4F-1** and **4F-2** are competing early-formed phases. Typically, a given crystallization vial yielded predominantly either **4F-1** or **4F-2** rather than a mixture of both phases. Variation of the MeOH/H_2O ratio, moderate concentration changes, and weakly acidic/weakly basic conditions did not provide reliable phase-selective control between **4F-1** and **4F-2**. Instead, repeated experiments indicated that these two

solids behave as competing early-formed phases under closely similar mother-liquor conditions. An empirical bias associated with subtle differences in the solution state prior to ether diffusion was observed: under relatively cooler ambient preparation conditions (ca. 12–20 °C), **4F-2** was more often obtained, whereas under relatively warmer conditions (ca. 20–30 °C), **4F-1** was more often obtained. No sharp phase-selective threshold is assigned here. Black plate-like crystals of **4F-2** suitable for single-crystal X-ray diffraction were isolated. Crystals of **4F-2** rapidly lose lattice solvent upon removal from the mother liquor; therefore, the isolated yield and empirical formula of the solvated crystalline phase are not reported here. When the crystals were isolated after 16 h of crystallization and subsequently dried under vacuum, the resulting desolvated **4F-2** sample weighed 16.4 mg (isolated in 26.8% yield based on Fe). Elemental analysis was performed on the dried sample and referenced to the desolvated framework composition. Anal. $C_{24}H_{20}F_4FeN_8O_4S_2$ (680.43); calcd: C, 42.36; H, 2.96; N, 16.47; found: C, 41.51; H, 3.22; N, 16.26. The observed CHN deviations are consistent with a small amount of residual moisture/solvent in the bulk sample after vacuum drying and/or minor moisture uptake during sample handling, which likely accounts for the small discrepancy between the observed and calculated CHN values.

Synthesis of $[Fe(HL)(L)]_2(4FTPA)\cdot(Et_2O)_2$ (4F-3)

Crystals of **4F-3** were obtained by leaving the initially formed **4F-1**/**4F-2** crystals standing in the oxygen-free mother liquor containing diethyl ether under N_2. After standing for ca. 16–24 h, the early-formed crystals gradually diminished and **4F-3** began to appear. After 5 d of standing, **4F-3** was isolated as black rod-/block-shaped crystals (31.0 mg, isolated in 54.2% yield based on Fe). At 293 K, the asymmetric unit comprises one $[Fe(HL)(L)]^+$ cation, one-half of a $4FTPA^{2-}$ anion located on a symmetry element, and one lattice Et_2O molecule. Anal. $C_{24}H_{29}F_2FeN_8O_3S_2$ (635.51); calcd: C, 45.36; H, 4.60; N, 17.63; found: C, 44.86; H, 4.15; N, 17.86.

Single-crystal X-ray diffraction (SCXRD)

Single-crystal X-ray diffraction data were collected on a Rigaku Oxford Diffraction diffractometer using graphite-monochromated Mo *Kα* radiation (λ = 0.71073 Å). Crystals were selected from the mother liquor, coated with an oil-based cryoprotectant, mounted on nylon loops, and immediately placed in a temperature-controlled stream of dry nitrogen gas during data collection. Data were collected at 100 K and at room temperature (293 K), as specified in the individual CIF files. Structures were solved by direct methods using SHELXT and refined by full-matrix least-squares on F^2 using SHELXL implemented in Olex2. Non-hydrogen atoms were refined anisotropically. Hydrogen atoms were placed in calculated

positions and refined using riding models with appropriate isotropic displacement parameters (as indicated by the CIF hydrogen treatment).

For **4F-2**, diffuse electron density from severely disordered lattice solvent in solvent-accessible voids was treated using the SQUEEZE[2] routine in PLATON;[3] therefore, the lattice-solvent contribution was excluded from the reported chemical formula and refinement tables.

1.3 Physical measurements and characterization

Magnetic Measurements

Solid-state magnetic susceptibility measurements were performed on a Quantum Design MPMS XL7 SQUID magnetometer under an applied dc field of 5000 Oe. Samples of **4F-1** and **4F-3** were prepared by encapsulating each crystalline compound in a gelatin capsule. To avoid efflorescence of the crystals by solvent loss, freshly prepared **4F-2** samples were sealed in a quartz tube under vacuum with a small amount of residual mother liquor. After the measurements were completed, the sample was recovered from the quartz tube and dried under vacuum at 100 °C for 24 h to determine the mass of the dried solid residue (m). The molar amount used for normalization was calculated as m/Mr, where Mr corresponds to the desolvated framework composition of **4F-2**, and this value was used to normalize the magnetic data. Phase identity of the recovered solid (**4F-1** after thermal cycling) was confirmed by PXRD/SCXRD. Diamagnetic corrections were applied based on Pascal's constants.

Hirshfeld Surface Analysis

Hirshfeld surfaces were generated using CrystalExplorer[4] to visualize intermolecular contacts. Surface mappings were calculated using standard van der Waals radii; short contacts appear as red regions on the surface. Calculations were performed from the crystallographic coordinates obtained by single-crystal X-ray diffraction.

Differential Scanning Calorimetry

Differential scanning calorimetry (DSC) measurements were carried out on a Differential Scanning Calorimeter PerkinElmer DSC 8000 under a nitrogen atmosphere.

Powder X-ray Diffraction

Powder X-ray diffraction (PXRD) data were recorded on a Shimadzu XRD-6000 diffractometer (Cu $K\alpha$ radiation, λ = 1.54056 Å) at room temperature.

Fourier Transform Infrared Spectroscopy

FT-IR spectra were recorded on a Bruker ALPHA ATR-IR in the range of 4000–400 cm^{-1} at room temperature (resolution 4 cm^{-1}; 24 scans). Data were processed using OPUS software.

Thermogravimetric Analysis

Thermogravimetric analysis (TGA) was performed on a NETZSCH STA 449F5 instrument under a nitrogen atmosphere from 20 to 1000 °C at a heating rate of 5 K min^{-1}.

1.4 Computational Methods

Based on the experimentally determined crystal structure of **4F-1**, cluster models representing the **Fe1A**-like and **Fe1B**-like local coordination environments were extracted. The initial geometries of the cluster models were taken directly from the experimental crystallographic coordinates, and the low-spin (LS) and high-spin (HS) states were each optimized at the density functional theory (DFT) level. Geometry optimizations were carried out using the reparametrized hybrid functional B3LYP*[5] (i.e., a B3LYP variant with the Hartree–Fock exact exchange adjusted to 15%) in combination with the split-valence triple-zeta polarized def2-TZVP basis set.[6] To describe the static correlation effects and the near-degeneracy of multiple electronic states within the Fe 3d manifold, state-averaged complete active space self-consistent field (CASSCF) calculations[7] were performed on the optimized cluster models using an active space of CAS(6,5), in which six active electrons were distributed among five metal 3d orbitals. The CASSCF calculations and the subsequent multireference treatments employed the def2-TZVPP basis set to improve the accuracy of the orbital and energy-level description, and were performed under TightSCF convergence criteria with the DefGrid3 numerical integration grid. On top of the CASSCF wavefunctions, second-order N-electron valence state perturbation theory (NEVPT2)[8] was used to include dynamic electron correlation. In view of the presence of multiple near-degenerate states in the system, quasi-degenerate NEVPT2 (QD-NEVPT2)[9] was further employed to allow for state coupling and to obtain more reliable energy-level ordering and excitation energies. Scalar relativistic effects were treated using the second-order Douglas–Kroll–Hess (DKH2) method.[10] Finally, ab initio ligand-field theory (AILFT)[11] was used to post-process the CASSCF/NEVPT2 wavefunctions and directly extract the metal 3d orbital energy levels, ligand-field matrix elements, and related ligand-field parameters. The ligand-field splitting energy was estimated according to

$$\Delta_{LF} = \frac{E_4 + E_5}{2} - \frac{E_1 + E_2 + E_3}{3}$$

All DFT and multireference calculations (CASSCF/NEVPT2, QD-NEVPT2, and AILFT) were carried out using the ORCA 6.1.1 program package.[12]

2. Additional Tables

2.1 4F-1 structural tables (Table S1–3)

Table S1. Crystal data and structure refinement for compound **4F-1**.

Complex	**4F-1** (100 K)	**4F-1** (293 K)
Empirical formula	$C_{48}H_{50}F_8Fe_2N_{16}O_{13}S_4$	$C_{24}H_{25}F_4FeN_8O_{6.5}S_2$
Formula weight	1450.98	725.49
Temperature / K	100.15	293(2)
Crystal system	Monoclinic	Monoclinic
Space group	$P2_1/n$	$P2_1/c$
a/Å	12.1782(3)	15.6714(6)
b/Å	16.6454(4)	16.6524(7)
c/Å	30.6968(7)	12.1681(4)
α/°	90	90
β/°	98.834(2)	98.772(3)
γ/°	90	90
Volume/Å^3	6148.8(3)	3138.3(2)
Z	4	4
$\rho_{calc.}$/g cm^{-3}	1.567	1.535
μ/mm^{-1}	0.705	0.691
F(000)	2968.0	1484.0
2θ range /°	4.176 to 61.952	7.112 to 58.678
Reflections collected	47933	36620
Independent reflections	15612 [R_{int} = 0.0334, R_{sigma} = 0.0377]	7429 [R_{int} = 0.0569, R_{sigma} = 0.0528]
Data/restraints/parameters	15612/19/866	7428/61/510
Goodness-of-fit on F^2	1.033	1.048
Final R indexes [$I \geq 2\sigma(I)$]	R_1 = 0.0460, wR_2 = 0.1093	R_1 = 0.0522, wR_2 = 0.1115
Final R indexes [all data]	R_1 = 0.0627, wR_2 = 0.1175	R_1 = 0.0861, wR_2 = 0.1206
Largest diff. peak/hole / e Å^{-3}	1.75/-1.06	0.26/-0.35
CCDC	2536440	2536441

[a]$R_1 = \Sigma||Fo| - |Fc||/\Sigma|Fo|$; [b]$wR_2 = [\Sigma w(Fo^2 - Fc^2)^2/\Sigma w(Fo^2)^2]^{1/2}$.

Table S2. Selected geometric parameters for **4F-1**.

	293 K (single site, HS)	100 K **Fe1A** (LS)	100 K **Fe1B** (HS)
Fe1–S1 (Å)	2.4899(10)	2.3295(7)	2.4694(6)
Fe1–S2 (Å)	2.5162(9)	2.3477(6)	2.5119(6)
Fe1–N1 (Å)	2.326(3)	2.123(2)	2.2923(19)
Fe1–N2 (Å)	2.234(2)	2.064(2)	2.2125(19)
Fe1–N3 (Å)	2.116(2)	1.939(2)	2.1229(19)
Fe1–N4 (Å)	2.130(2)	1.933(2)	2.1268(18)
Σ (°)	127.5964	82.0722	128.1894

Table S3. Hydrogen-bond geometry for **4F-1**.

	293 K (component **X**)		293 K (component **Y**)		100 K **Fe1A** (LS)		100 K **Fe1B** (HS)	
	D···A (Å)	∠D–H···A (°)	D···A (Å)	∠D–H···A (°)	D···A (Å)	∠D–H···A (°)	D···A (Å)	∠D–H···A (°)
C7···O1	3.171(8)	133.9	3.233(7)	140.1	—	—	3.174(2)	142.0
N5···O1	2.765(7)	156(3)	3.341(8)	141(3)	2.693(3)	170(3)	—	—
N5···O2	3.259(8)	146(3)	2.775(9)	161(3)	—	—	2.744(3)	170(3)
N7···O2	2.961(9)	164(4)	3.041(10)	145(4)	2.854(3)	170(3)	—	—
N6···O3	2.689(3)	173(3)	2.689(3)	172(3)	2.675(3)	173(3)	2.657(2)	173(3)
N8···O4	2.882(3)	158(3)	2.882(3)	158(3)	2.839(3)	164(3)	2.917(3)	165(3)

2.2 4F-2 structural tables (Table S4–6)

Table S4. Crystal data and structure refinement for compound **4F-2**.

Complex	**4F-2** (100K)	**4F-2** (293K)
Empirical formula	$C_{24}H_{20}F_4FeN_8O_4S_2$	$C_{24}H_{20}F_4FeN_8O_4S_2$
Formula weight	680.45	680.45
Temperature / K	100.15	293(2)
Crystal system	Monoclinic	Monoclinic
Space group	*C*2/*c*	*C*2/*c*
a/Å	23.4820(8)	22.8595(10)
b/Å	10.9461(3)	11.4174(4)
c/Å	26.9252(8)	28.0459(11)
α/°	90	90
β/°	113.386(4)	113.106(5)
γ/°	90	90
Volume/Å^3	6352.2(4)	6732.7(5)
Z	8	8
$\rho_{calc.}$/g cm^{-3}	1.423	1.343
μ/mm^{-1}	0.672	0.634
F(000)	2768.0	2768.0
2θ range /°	4.174 to 62.136	3.874 to 62.276
Reflections collected	22941	42559
Independent reflections	7920 [R_{int} = 0.0289, R_{sigma} = 0.0315]	9052 [R_{int} = 0.0367, R_{sigma} = 0.0314]
Data/restraints/parameters	7920/15/408	9052/15/408
Goodness-of-fit on F^2	1.068	1.088
Final *R* indexes [$I \geq 2\sigma$ (*I*)]	R_1 = 0.0361, wR_2 = 0.0903	R_1 = 0.0355, wR_2 = 0.0967
Final *R* indexes [all data]	R_1 = 0.0461, wR_2 = 0.0942	R_1 = 0.0521, wR_2 = 0.1022
Largest diff. peak/hole / e Å^{-3}	0.82/-0.61	0.35/-0.24
CCDC	2536442	2536443

[a]$R_1 = \Sigma||Fo| - |Fc||/\Sigma|Fo|$; [b]$wR_2 = [\Sigma w(Fo^2 - Fc^2)^2/\Sigma w(Fo^2)^2]^{1/2}$.

Table S5. Selected geometric parameters for **4F-2**.

	293 K (HS)	100 K (LS)
Fe1–S1 (Å)	2.4969(5)	2.3001(5)
Fe1–S2 (Å)	2.4985(5)	2.2829(5)
Fe1–N1 (Å)	2.2472(14)	2.0507(15)
Fe1–N2 (Å)	2.2229(13)	2.0323(15)
Fe1–N3 (Å)	2.1164(12)	1.9014(14)
Fe1–N4 (Å)	2.1339(12)	1.8980(14)
Σ (°)	136.5071	74.7056

Table S6. Hydrogen-bond geometry for **4F-2**.

	293 K (HS)		100 K (LS)	
	D···A (Å)	∠D–H···A (°)	D···A (Å)	∠D–H···A (°)
N5···O1	2.6819(18)	170(2)	2.668(2)	172(2)
N7···O2	2.840(2)	169(2)	2.8267(19)	168(2)
N6···O3	2.6889(17)	171.8(19)	2.6908(19)	173(2)
N8···O4	2.8189(18)	173.3(19)	2.7960(19)	170(2)

2.3 4F-3 structural tables (Table S7–10)

Table S7. Crystal data and structure refinement for compound **4F-3**.

Complex	**4F-3** (100K)	**4F-3** (293K)
Empirical formula	$C_{48}H_{58}F_4Fe_2N_{16}O_6S_4$	$C_{24}H_{29}F_2FeN_8O_3S_2$
Formula weight	1271.04	635.52
Temperature / K	100.15	293(2)
Crystal system	Triclinic	Triclinic
Space group	$P\bar{1}$	$P\bar{1}$
a/Å	14.8054(4)	8.2306(2)
b/Å	15.3522(4)	13.2874(4)
c/Å	15.4097(5)	14.9297(6)
α/°	62.938(3)	116.125(4)
β/°	61.952(3)	100.097(3)
γ/°	73.208(2)	91.106(2)
Volume/Å^3	2740.20 (17)	1434.62(9)
Z	2	2
$\rho_{calc.}$/g cm^{-3}	1.540	1.471
μ/mm^{-1}	0.760	0.726
F(000)	1316.0	658.0
2θ range /°	7.198 to 58.712	7.162 to 58.07
Reflections collected	55541	23556
Independent reflections	13028 [R_{int} = 0.0369, R_{sigma} = 0.0364]	6620 [R_{int} = 0.0365, R_{sigma} = 0.0381]
Data/restraints/parameters	13028/13/759	6620/52/400
Goodness-of-fit on F^2	1.032	1.059
Final R indexes [$I \geq 2\sigma$ (I)]	R_1 = 0.0359, wR_2 = 0.0848	R_1 = 0.0357, wR_2 = 0.0897
Final R indexes [all data]	R_1 = 0.0521, wR_2 = 0.0914	R_1 = 0.0505, wR_2 = 0.0958
Largest diff. peak/hole / e Å^{-3}	0.80/-0.45	0.46/-0.37
CCDC	2549382	2549369

[a]$R_1 = \Sigma||Fo| - |Fc||/\Sigma|Fo|$; [b]$wR_2 = [\Sigma w(Fo^2 - Fc^2)^2/\Sigma w(Fo^2)^2]^{1/2}$.

Table S8. Selected geometric parameters for **4F-3**.

	293 K (single site, HS)	100 K **Fe1A** (LS)	100 K **Fe1B** (HS)
Fe1–S1 (Å)	2.4428(5)	2.2965(5)	2.4427(5)
Fe1–S2 (Å)	2.5037(5)	2.3059(5)	2.4848(5)
Fe1–N1 (Å)	2.2402(15)	2.0488(16)	2.2275(16)
Fe1–N2 (Å)	2.2628(15)	2.0666(16)	2.2492(16)
Fe1–N3 (Å)	2.1340(14)	1.9358(15)	2.1294(15)
Fe1–N4 (Å)	2.1657(14)	1.9015(15)	2.1652(15)
Σ (°)	133.0989	81.9648	133.8367

Table S9. Hydrogen-bond geometry for **4F-3**.

	293 K (single site, HS)		100 K **Fe1A** (LS)		100 K **Fe1B** (HS)	
	D···A (Å)	∠D–H···A (°)	D···A (Å)	∠D–H···A (°)	D···A (Å)	∠D–H···A (°)
N6···O1	2.599(2)	176(2)	2.578(2)	171(2)	2.610(2)	176(2)
N8···O2	2.875(2)	169(3)	2.909(2)	169(2)	2.873(2)	172(2)

Table S10. Geometrical parameters of hydrogen-bond in **4F-3**.

	293 K Fe (HS)	100 K **Fe1A** (LS)	100 K **Fe1B** (HS)
N6···O1 (Å)	2.599(2)	2.578(2)	2.610(2)
C-O (Å)	1.247(3)	1.267(3)	1.262(2)
C=O (Å)	1.221(3)	1.231(3)	1.234(3)
∠NNC (°)	118.50(15)	116.66(15)	117.64(15)

3. Additional Figures

3.1 Phase transformation and phase validation (Figures S1–S2)

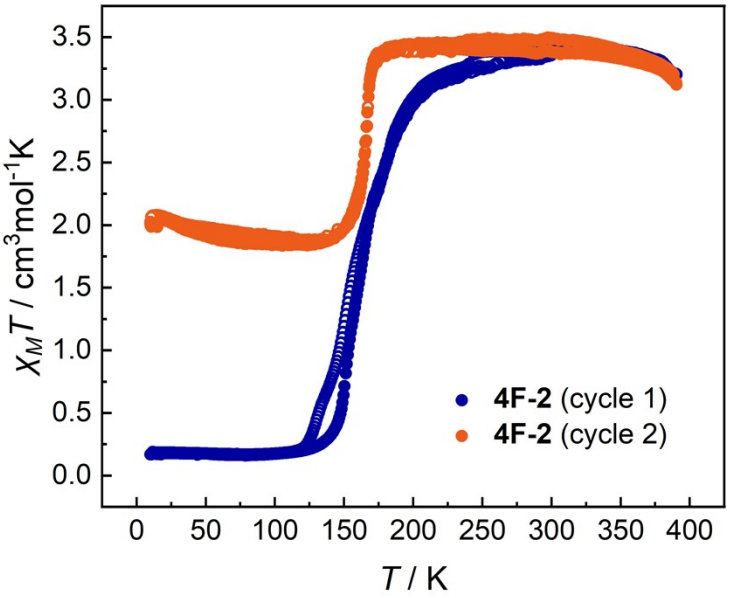

Figure S1. Temperature dependence of $\chi_M T$ measured in a continuous experiment comprising two thermal cycles. Cycle 1 (blue; open circles = cooling, filled circles = heating) corresponds to the first scan 300 → 10 → 390 K and represents phase **4F-2**. After holding the sample at 390 K for 10 min, the material converts to phase **4F-1**. Cycle 2 (orange; open circles = cooling, filled circles = heating) recorded during the subsequent 390 → 10 → 390 K scan follows the magnetic behavior of **4F-1**.

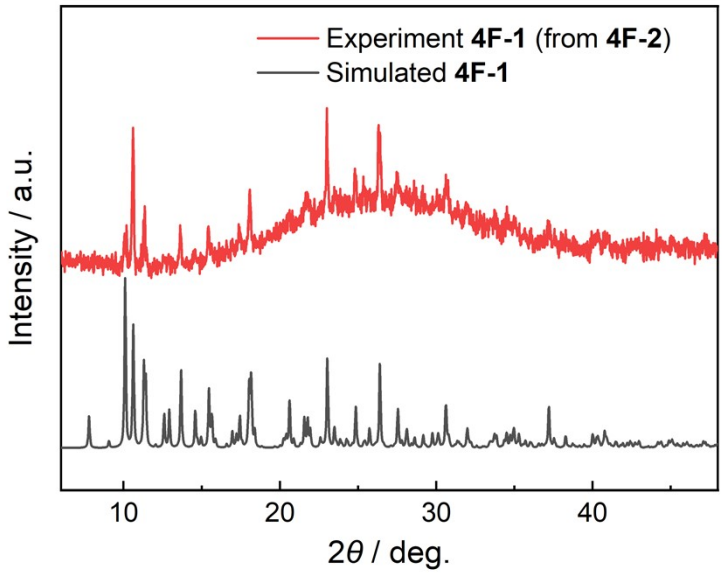

Figure S2. Experimental PXRD pattern of the sample recovered from **4F-2** after the second magnetic susceptibility cycle to 390 K, compared with the simulated PXRD pattern of **4F-1**. The good agreement between the two patterns confirms the **4F-2** → **4F-1** transformation under the magnetic measurement conditions.

3.2 4F-1 structural analysis (Figures S3–S8)

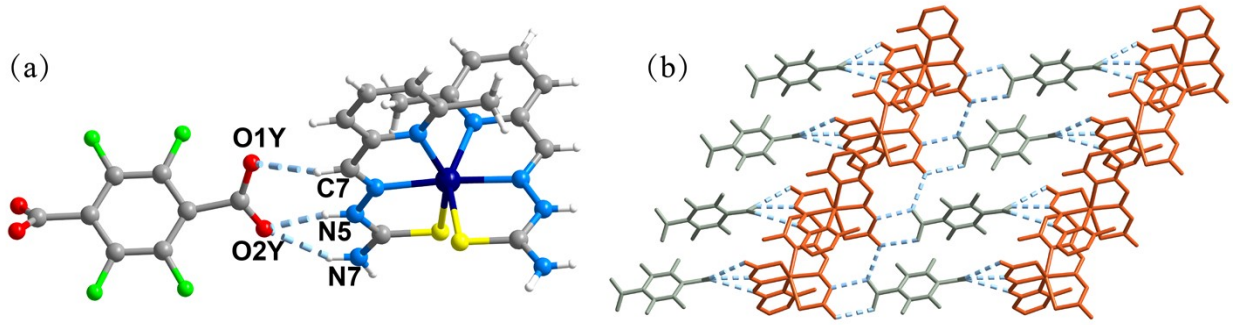

Figure S3. (a) Cation–anion hydrogen-bonding environment at 293 K (component Y). (b) Hydrogen-bonded 2D layer at 293 K (all HS, component Y).

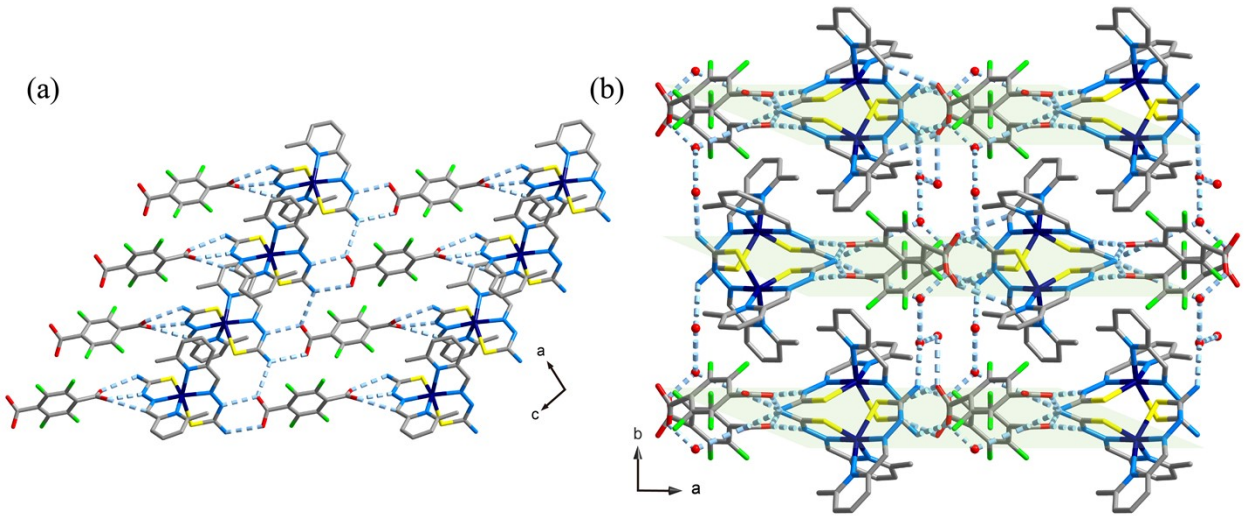

Figure S4. Hydrogen-bonded architecture of **4F-1** at 293 K. (a) One-dimensional cation–anion chains associate through interchain hydrogen bonds to form two-dimensional layers. (b) View of the three-dimensional hydrogen-bond network, in which neighboring layers (green) are bridged by lattice water molecules (shown as red spheres). Hydrogen bonds are shown as dashed lines. Hydrogen atoms are omitted for clarity. For clarity, the packing views are drawn using component X of the room-temperature disorder; the X/Y disorder affects the local hydrogen-bonding details but does not alter the overall packing topology.

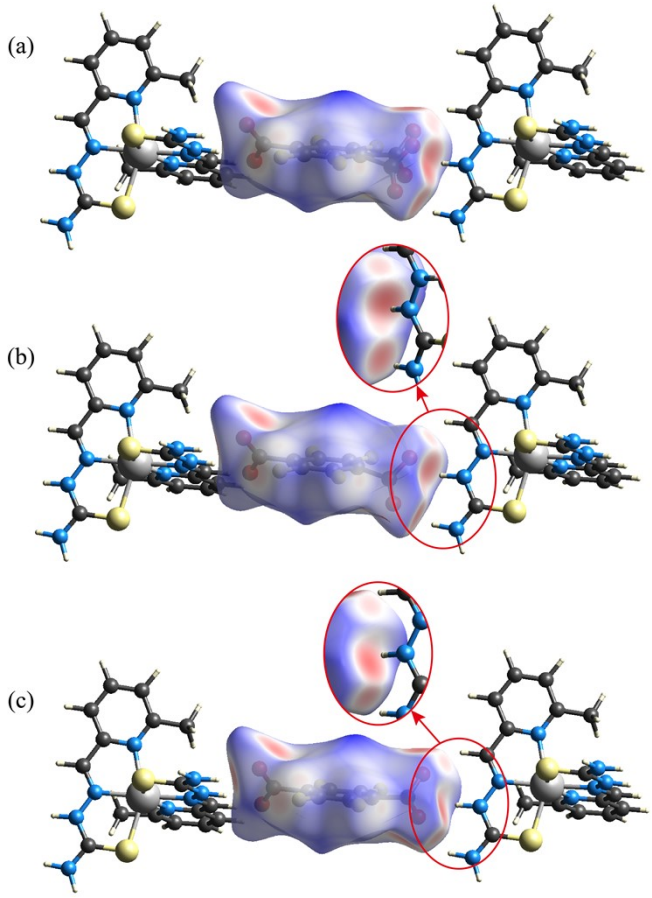

Figure S5. Hirshfeld surface analysis of **4F-1** at 293 K. (a) Hirshfeld surface calculated from the original disordered 293 K structure. (b) Hirshfeld surface calculated from an idealized model in which component X is fixed at full occupancy. (c) Hirshfeld surface calculated from an idealized model in which component Y is fixed at full occupancy.

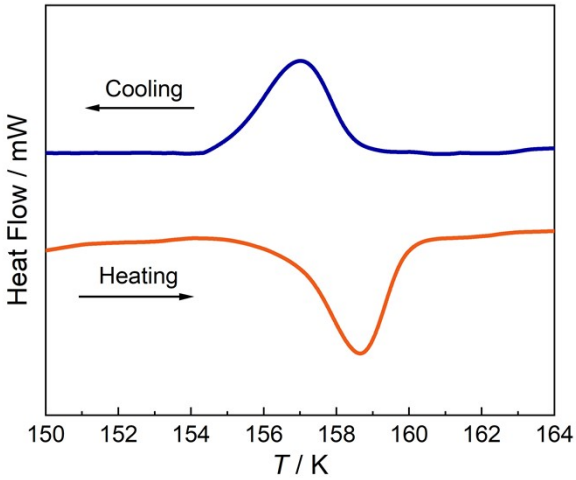

Figure S6. Differential scanning calorimetry (DSC) curves of **4F-1** recorded during cooling (blue) and heating (orange) cycles at a scan rate of 10 K min^{-1}. Well-defined exothermic and endothermic anomalies are observed at 157 K on cooling and 158.7 K on heating, respectively, close to the temperatures of the magnetic transition.

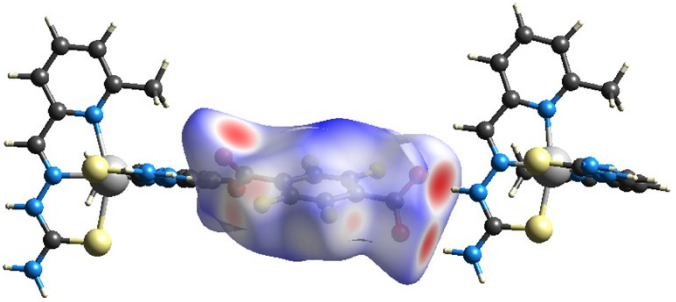

Figure S7. Hirshfeld surface of **4F-1** at 100 K (**Fe1A**, LS)

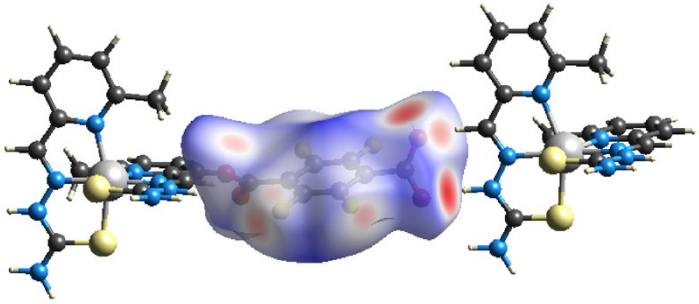

Figure S8. Hirshfeld surface of **4F-1** at 100 K (**Fe1B**, HS).

3.3 4F-3 structural and thermal analysis (Figures S9–S11)

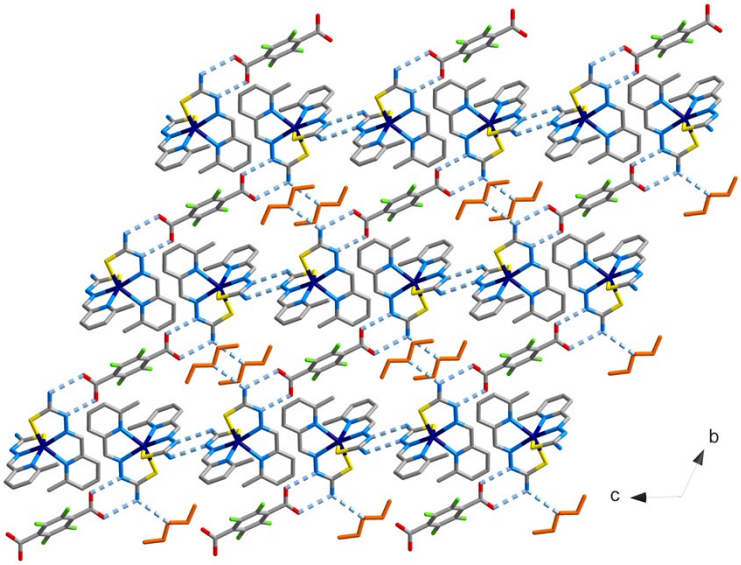

Figure S9. Packing view of **4F-3** along the *a* axis. Lattice Et_2O molecules are shown in orange; hydrogen atoms are omitted for clarity.

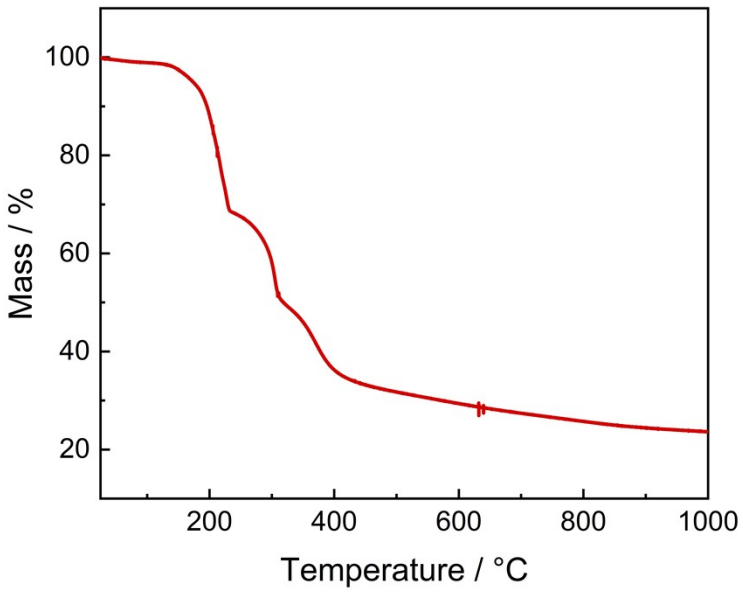

Figure S10. TGA of **4F-3**. No distinct low-temperature mass-loss step is observed below ca. 200 °C, consistent with the robust retention of lattice Et_2O.

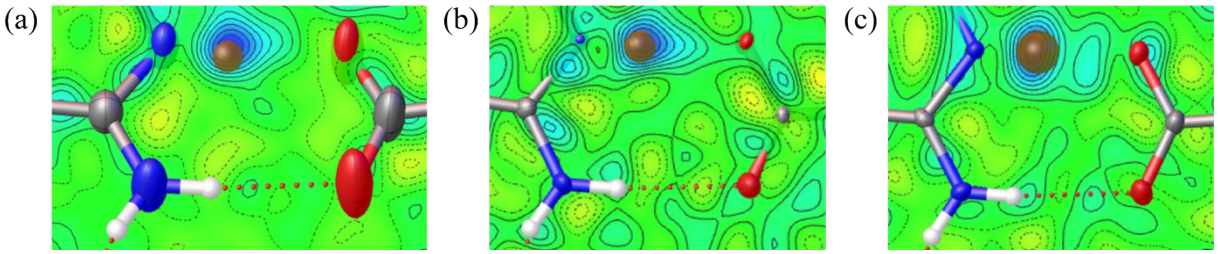

Figure S11. Difference Fourier maps for **4F-3** showing the residual electron-density distribution in the vicinity of the H6 proton. (a) 293 K. (b) 100 K, **Fe1A** site. (c) 100 K, **Fe1B** site. The residual density indicates that the H6 proton is located closer to the ligand N atom.

3.4 Computational analysis (Figures S12–S13)

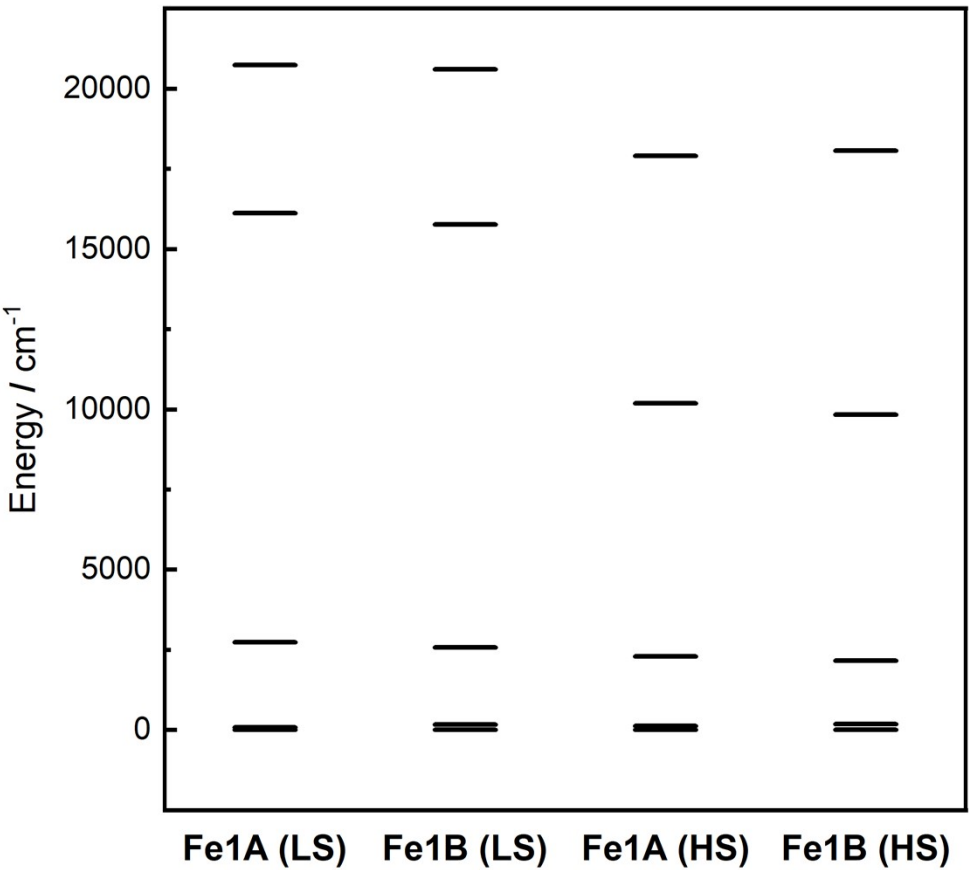

Figure S12. d-Orbital energies derived from AILFT ligand-field analysis based on CASSCF calculations for the **Fe1A**-like and **Fe1B**-like cluster models in the LS and HS geometries. The effective ligand-field splitting, estimated from the average energies of the upper two and lower three d orbitals, is slightly larger for **Fe1A** than for **Fe1B** in both geometries: 17486.1 vs 17269.7 cm^{-1} in the LS geometry and 13245.0 vs 13176.4 cm^{-1} in the HS geometry. These results indicate a slightly stronger effective ligand field for **Fe1A**, consistent with its greater tendency to stabilize the LS state.

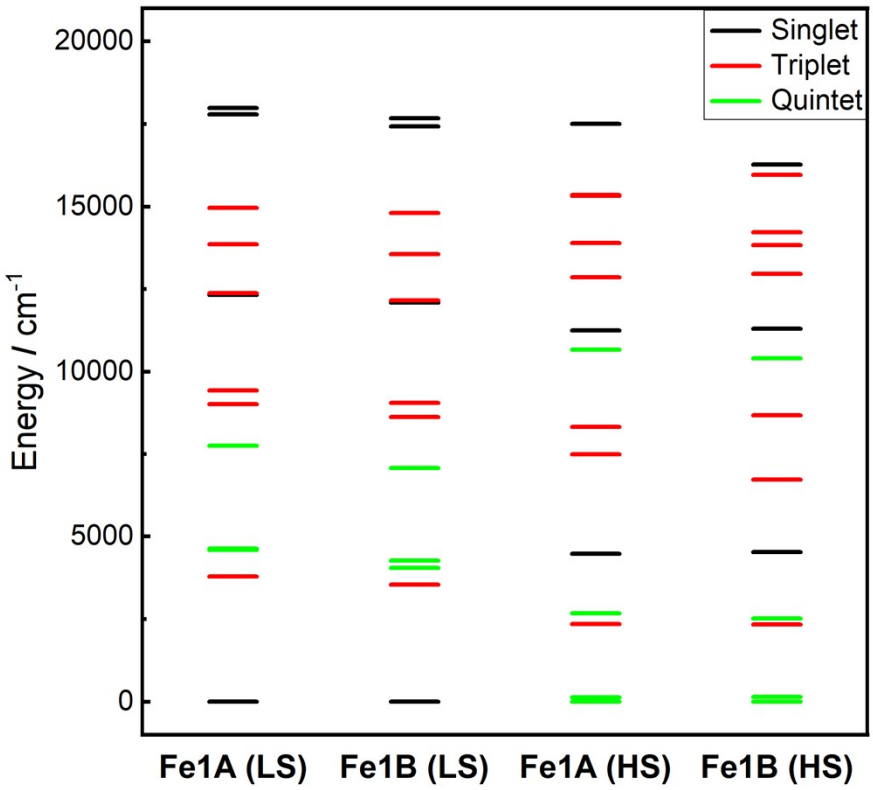

Figure S13. Low-lying electronic states derived from QD-NEVPT2 calculations for the **Fe1A**-like and **Fe1B**-like cluster models in the LS and HS geometries. Black, red, and green lines denote singlet, triplet, and quintet states, respectively. These results support a greater tendency for LS stabilization for **Fe1A**, while **Fe1B** is comparatively more compatible with the HS state.

3.5 4F-3 thermal analysis (Figure S14)

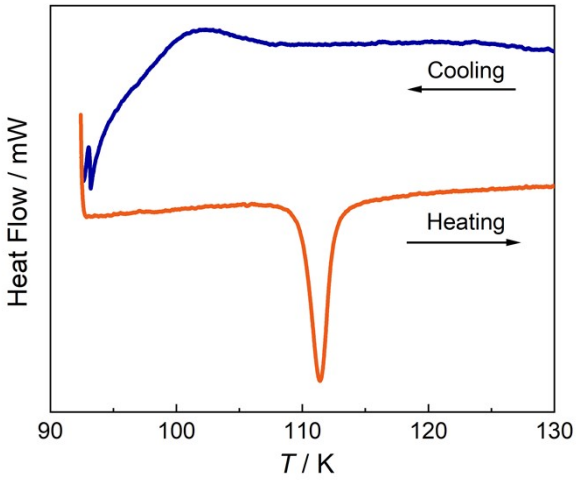

Figure S14. Differential scanning calorimetry (DSC) traces of 4F-3 recorded during cooling and heating at a scan rate of 2 K min^{-1}. A reproducible endothermic anomaly is observed at approximately 113 K on heating, corresponding to the reverse spin crossover transition. On cooling, a broad and weak thermal feature is discernible near the expected transition range; however, because it remains poorly resolved and lies close to the low-temperature limit of the DSC measurement window, no definitive cooling DSC transition temperature is assigned.

3.6 Powder X-ray diffraction (Figures S15–S17)

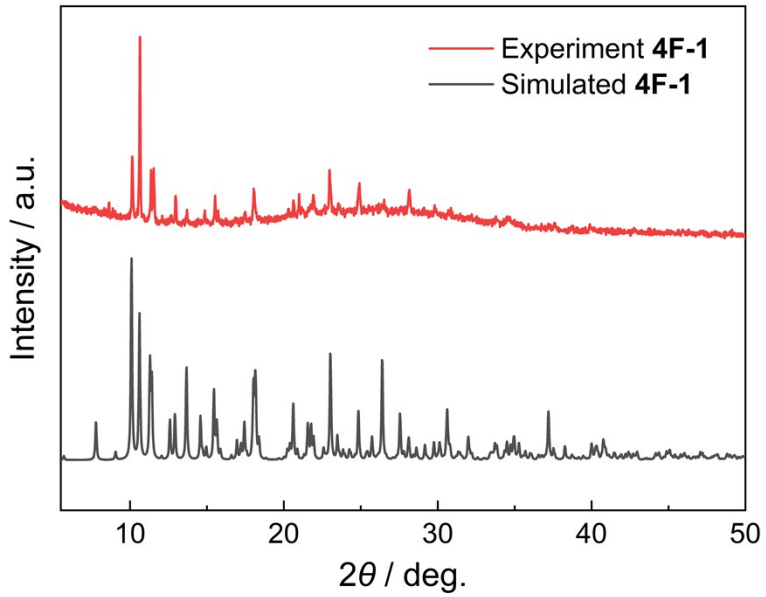

Figure S15. PXRD patterns of **4F-1** at room temperature.

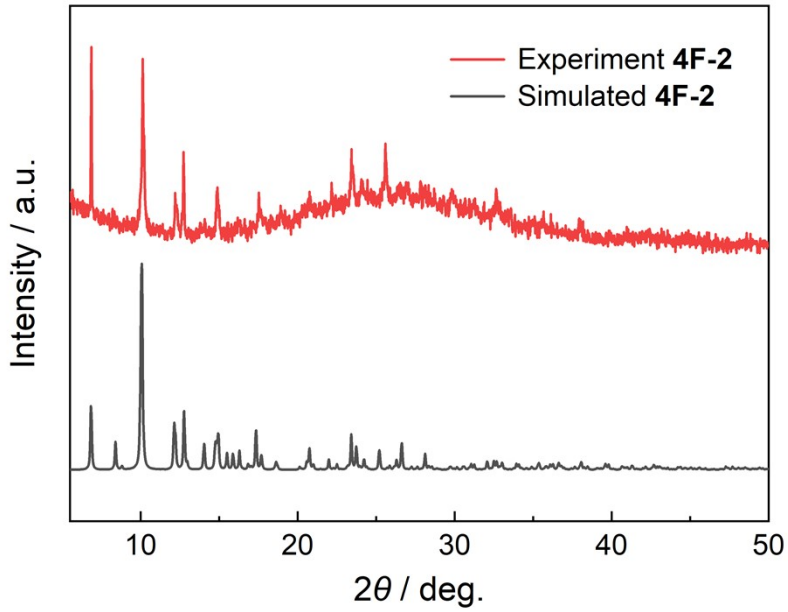

Figure S16. PXRD patterns of **4F-2** at room temperature. The experimental pattern was collected from the vacuum-dried sample, and the simulated pattern was generated from the solvent-free structural model used for the dried phase.

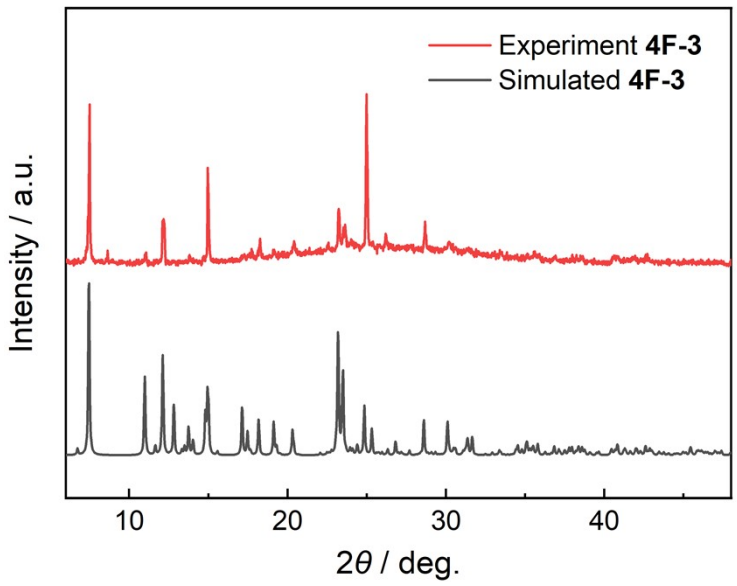

Figure S17. PXRD patterns of **4F-3** at room temperature.

3.7 Additional thermal and spectroscopic characterization (Figures S18–S20)

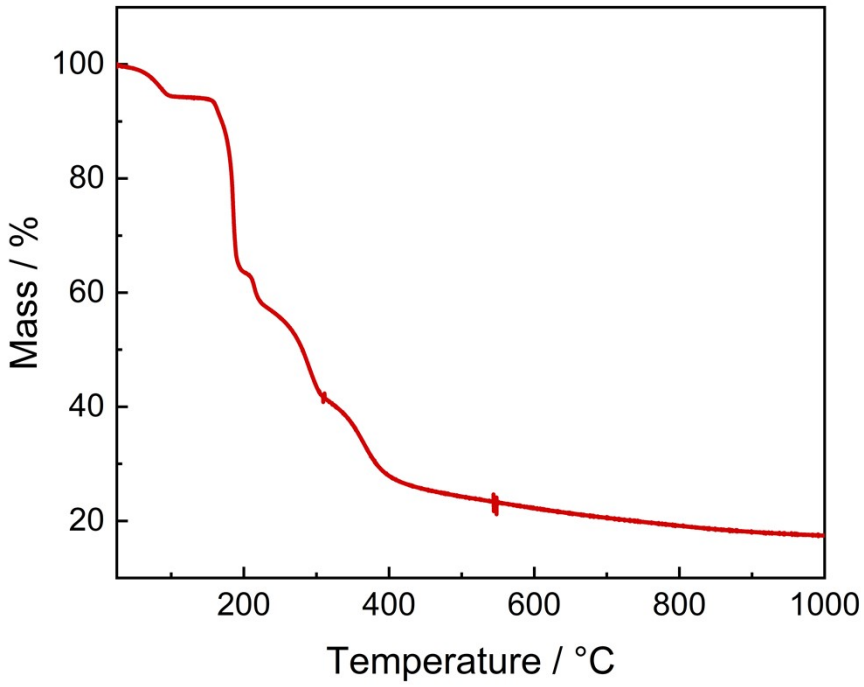

Figure S18. TGA of **4F-1**.

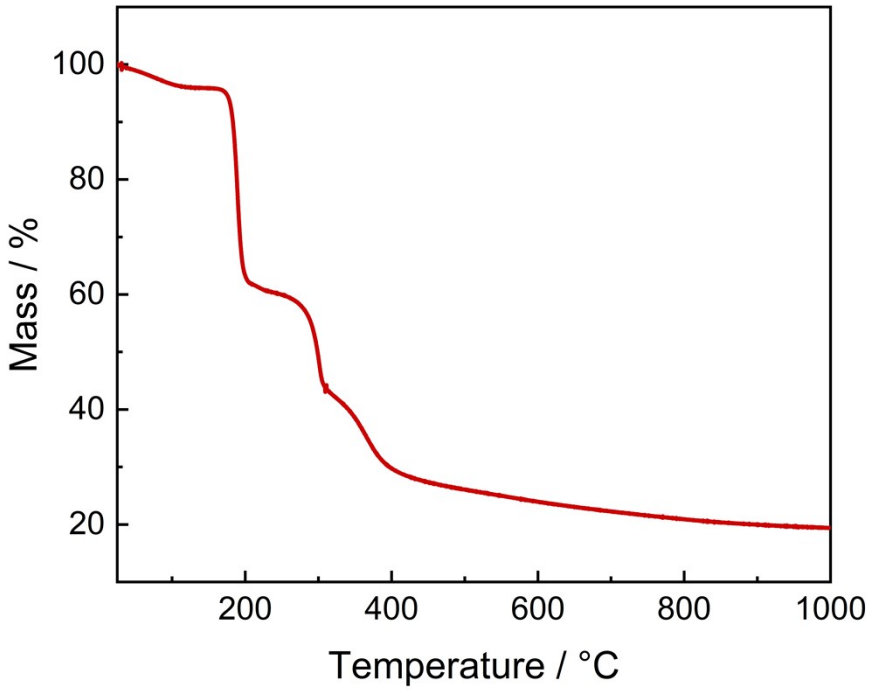

Figure S19. TGA of **4F-2**.

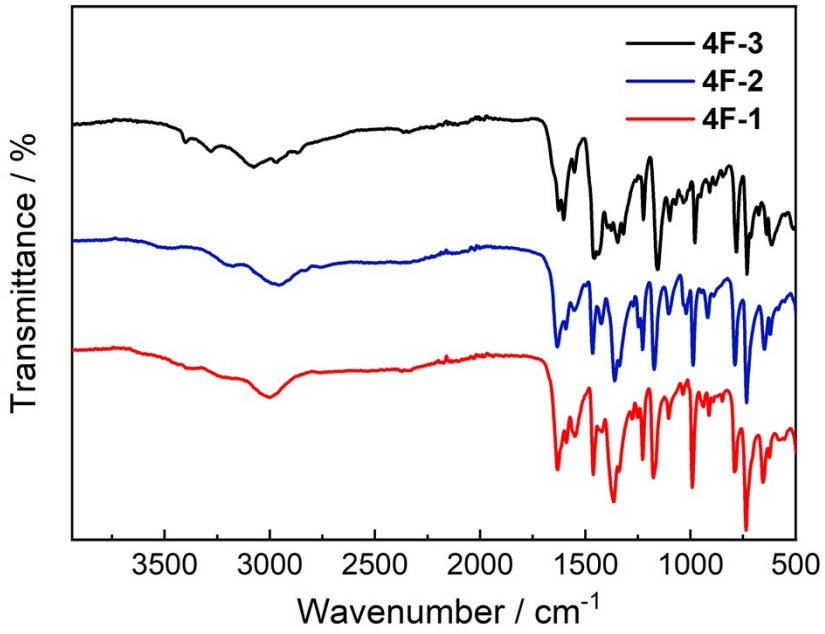

Figure S20. FT-IR spectra recorded at 298 K.

References

1. D. X. West, S. L. Dietrich, I. Thientanavanich, C. A. Brown and A. E. Liberta, Copper(II) complexes of 6-methyl-2-formylpyridine 4N-substituted thiosemicarbazones, *Transition Met. Chem.*, 1994, **19**, 195-200.
2. A. L. Spek, PLATON SQUEEZE: a tool for the calculation of the disordered solvent contribution to the calculated structure factors, *Acta Crystallogr., Sect. C: Struct. Chem.*, 2015, **71**, 9-18.
3. A. L. Spek, Structure validation in chemical crystallography, *Acta Crystallogr., Sect. D: Biol. Crystallogr.*, 2009, **65**, 148-155.
4. P. R. Spackman, M. J. Turner, J. J. McKinnon, S. K. Wolff, D. J. Grimwood, D. Jayatilaka and M. A. Spackman, CrystalExplorer: a program for Hirshfeld surface analysis, visualization and quantitative analysis of molecular crystals, *J. Appl. Crystallogr.*, 2021, **54**, 1006-1011.
5. O. Salomon, M. Reiher and B. A. Hess, Variation of the average ligand-field strength as a function of the Hartree–Fock exchange contribution in reparametrized density functionals, *J. Chem. Phys.*, 2002, **117**, 4729-4737.
6. F. Weigend and R. Ahlrichs, Balanced basis sets of split valence, triple zeta valence and quadruple zeta valence quality for H to Rn: Design and assessment of accuracy, *Phys. Chem. Chem. Phys.*, 2005, **7**, 3297-3305.
7. B. O. Roos, P. R. Taylor and P. E. M. Siegbahn, A complete active space SCF method (CASSCF) using a density matrix formulated super-CI approach, *Chem. Phys.*, 1980, **48**, 157-173.
8. C. Angeli, R. Cimiraglia and J. P. Malrieu, n-electron valence state perturbation theory: A spinless formulation and an efficient implementation of the strongly contracted and of the partially contracted variant, *J. Chem. Phys.*, 2002, **117**, 9138-9153.
9. J. W. Park, Analytical Gradient Theory for Quasidegenerate N-Electron Valence State Perturbation Theory (QD-NEVPT2), *J. Chem. Theory Comput.*, 2020, **16**, 326-339.
10. M. Reiher, Relativistic Douglas–Kroll–Hess theory, *Wiley Interdiscip. Rev. Comput. Mol. Sci.*, 2012, **2**, 139-149.
11. S. K. Singh, J. Eng, M. Atanasov and F. Neese, Covalency and chemical bonding in transition metal complexes: An ab initio based ligand field perspective, *Coord. Chem. Rev.*, 2017, **344**, 2-25.
12. F. Neese, The ORCA program system, *Wiley Interdiscip. Rev. Comput. Mol. Sci.*, 2012, **2**, 73-78.